Science

AAAS

Pacific Ocean Heat Content During the Past 10,000 Years
Yair Rosenthal *et al.*
Science **342**, 617 (2013);
DOI: 10.1126/science.1240837

This copy is for your personal, non-commercial use only.

interfaces do not contact any polymer throughout the process, reducing impurities trapped between the layers. Figure 2C shows an atomic force microscope (AFM) image of a BN-G-BN heterostructure made by vdW assembly. The graphene appears clean and free of macroscopic contamination over the entire device area, $\sim$200 μm^2. In Fig. 2D, a high-resolution cross section STEM image shows that the resulting interface is pristine down to the atomic scale, with the graphene layer nearly indistinguishable from the adjacent BN lattice planes.

Figure 3A shows electrical transport from a large-area, 15 $\mu m \times$ 15 μm, BN-G-BN device fabricated by combining vdW assembly with edge-contacts. The transport characteristics indicate the graphene device to be remarkably pristine, reaching a room-temperature mobility in excess of 140,000 cm^2/Vs. At carrier density $|n| = 4.5 \times 10^{12}$ cm^{-2}, the sheet resistivity is less than $\sim$40 ohms per square (fig. S13), corresponding to an equivalent 3D resistivity below 1.5 $\mu ohm \cdot cm$, smaller than the resistivity of any metal at room temperature. Indeed, the remarkable feature of this device response is the simultaneous realization of both high mobility and large carrier density. Using the simple Drude model of conductivity, $\sigma = ne\mu$, where μ is the electron mobility, we calculate a mobility of $\sim$40, 000 cm^2/Vs at densities as large as $n \sim 4.5 \times 10^{12}$ cm^{-2}. In this high-density regime, the measured mobility is comparable to the acoustic-phonon-limited mobility theoretically predicted for intrinsic graphene (28, 29). The room-temperature response of the graphene device reported here outperforms all other 2D materials, including the highest mobility 2D heterostructures fabricated from III-V (groups III and V in the periodic table) semiconductors (30, 31) (Fig. 3B) by at least a factor of 2 over the entire range of technologically relevant carrier densities.

At low temperatures, four-terminal measurement yields a negative resistance (inset in Fig. 3A), indicating quasiballistic transport (4) over at least 15 μm. In the diffusive regime, the mean free path, L_{mfp}, can be calculated from the conductivity, σ, according to $L_{mfp} = \sigma h/2e^2 k_F$ where $k_F = \sqrt{\pi n}$ is the Fermi wave vector. In Fig. 3C, L_{mfp} versus applied gate voltage is shown for selected temperatures from 300 K down to 20 K. The mean free path increases with gate voltage until it saturates at a temperature-dependent value at high density. This maximum L_{mfp} increases monotonically with decreasing temperature until the mean free path approaches the device size at T $\sim$ 40 K (Fig. 3D). In the low-temperature ballistic regime, four-terminal measurement is dominated by mesoscopic effects (32) and the calculated mean free path exhibits large variation, depending on the measurement geometry. The temperature dependence therefore provides only a lower bound of the mean free path.

The negative resistance observed at base temperature indicates that electrons travel ballistically across the diagonal of the square, corresponding to a mean free path as large as 21 μm in this device. This value corresponds to an electron mobility of $\sim$1,000,000 cm^2/Vs at a carrier density of $\sim$3 $\times$ 10^{12} cm^{-2}. We repeated this measurement for devices varying in size from 1 to 15 μm. As seen in Fig. 3E, the maximum mean free path scales linearly with device size. This result indicates that in our devices the low-temperature mobility is limited by the available crystal size, and we have not reached the intrinsic impurity-limited scattering length. Even higher mobility could be expected for larger-area devices, which may be realized by combining recent progress in scalable growth techniques (33, 34) together with the edge-contact geometry described here.

References and Notes

1. M. Xu, T. Liang, M. Shi, H. Chen, *Chem. Rev.* **113**, 3766–3798 (2013).
2. A. K. Geim, I. V. Grigorieva, *Nature* **499**, 419–425 (2013).
3. C. R. Dean *et al.*, *Nat. Nanotechnol.* **5**, 722–726 (2010).
4. A. S. Mayorov *et al.*, *Nano Lett.* **11**, 2396–2399 (2011).
5. L. Wang *et al.*, *ACS Nano* **6**, 9314–9319 (2012).
6. C. R. Dean *et al.*, *Nature* **497**, 598–602 (2013).
7. L. A. Ponomarenko *et al.*, *Nature* **497**, 594–597 (2013).
8. B. Hunt *et al.*, *Science* **340**, 1427–1430 (2013).
9. L. Britnell *et al.*, *Science* **335**, 947–950 (2012).
10. T. Georgiou *et al.*, *Nat. Nanotechnol.* **8**, 100–103 (2013).
11. L. Britnell *et al.*, *Science* **340**, 1311–1314 (2013).
12. G. Giovannetti *et al.*, *Phys. Rev. Lett.* **101**, 026803 (2008).
13. C. Gong *et al.*, *J. Appl. Phys.* **108**, 123711 (2010).
14. F. Léonard, A. A. Talin, *Nat. Nanotechnol.* **6**, 773–783 (2011).
15. F. Xia, V. Perebeinos, Y. M. Lin, Y. Wu, P. Avouris, *Nat. Nanotechnol.* **6**, 179–184 (2011).
16. M. S. Choi, S. H. Lee, W. J. Yoo, *J. Appl. Phys.* **110**, 073305 (2011).
17. D. Berdebes, T. Low, Y. Sui, J. Appenzeller, M. S. Lundstrom, *IEEE Trans. Electron. Dev.* **58**, 3925–3932 (2011).
18. J. S. Moon *et al.*, *Appl. Phys. Lett.* **100**, 203512 (2012).
19. J. T. Smith, A. D. Franklin, D. B. Farmer, C. D. Dimitrakopoulos, *ACS Nano* **7**, 3661–3667 (2013).
20. M. Ishigami, J. H. Chen, W. G. Cullen, M. S. Fuhrer, E. D. Williams, *Nano Lett.* **7**, 1643–1648 (2007).
21. J. A. Robinson *et al.*, *Appl. Phys. Lett.* **98**, 053103 (2011).
22. J. Yamaguchi, K. Hayashi, S. Sato, N. Yokoyama, *Appl. Phys. Lett.* **102**, 143505 (2013).
23. N. Lindvall, A. Kalabukhov, A. Yurgens, *J. Appl. Phys.* **111**, 064904 (2012).
24. S. J. Haigh *et al.*, *Nat. Mater.* **11**, 764–767 (2012).
25. Y. Matsuda, W.-Q. Deng, W. A. Goddard III, *J. Phys. Chem. C* **114**, 17845–17850 (2010).
26. K. Cho *et al.*, *MRS Proc.* **1259**, S14–S35 (2010).
27. Y. Wu *et al.*, *AIP Adv.* **2**, 012132 (2012).
28. E. Hwang, S. Das Sarma, *Phys. Rev. B* **77**, 115449 (2008).
29. J. H. Chen, C. Jang, S. Xiao, M. Ishigami, M. S. Fuhrer, *Nat. Nanotechnol.* **3**, 206–209 (2008).
30. B. R. Bennett, R. Magno, J. B. Boos, W. Kruppa, M. G. Ancona, *Sol. Stat. Elec.* **49**, 1875–1895 (2005).
31. J. Orr *et al.*, *Phys. Rev. B* **77**, 165334 (2008).
32. S. Datta, *Electronic Transport in Mesoscopic Systems* (Cambridge Univ. Press, London, 1995).
33. W. Yang *et al.*, *Nat. Mater.* **12**, 792–797 (2013).
34. Z. Liu *et al.*, *Nano Lett.* **11**, 2032–2037 (2011).

Pacific Ocean Heat Content During the Past 10,000 Years

Yair Rosenthal,[1]* Braddock K. Linsley,[2] Delia W. Oppo[3]

Observed increases in ocean heat content (OHC) and temperature are robust indicators of global warming during the past several decades. We used high-resolution proxy records from sediment cores to extend these observations in the Pacific 10,000 years beyond the instrumental record. We show that water masses linked to North Pacific and Antarctic intermediate waters were warmer by 2.1 $\pm$ 0.4°C and 1.5 $\pm$ 0.4°C, respectively, during the middle Holocene Thermal Maximum than over the past century. Both water masses were $\sim$0.9°C warmer during the Medieval Warm period than during the Little Ice Age and $\sim$0.65° warmer than in recent decades. Although documented changes in global surface temperatures during the Holocene and Common era are relatively small, the concomitant changes in OHC are large.

Small, yet persistent perturbations in the balance of incoming solar radiation (insolation) reaching Earth's surface and outgoing long-wave radiation can lead to substantial climate change. Nevertheless, relating climate variations to radiative perturbations is not straightforward due to the inherent noise of the system caused by large temporal (seasonal to decadal) and spatial variability of the climatic response. A long-term perspective of climate variability relative to known radiative perturbations can place the recent trends in the broader framework of natural variability. The comparison with paleoclimate reconstructions of surface temperatures

is, however, complicated because of the limited number of proxy records, their uneven geographical distribution, and the seasonal ecological biases of the proxies (1, 2).

Globally averaged instrumental surface temperatures have registered little increase in recent decades, despite a considerable imbalance in the planetary energy budget (3). The apparent discrepancy is attributed to the warming of the ocean's interior over the same period. Instrumental records show that the increase in ocean heat content (OHC) accounts for ~90% of the expected warming of Earth, thereby demonstrating that OHC more reliably represents the response of Earth's energy budget to radiative perturbations than do surface temperatures (4–6). Furthermore, subsurface water masses are directly ventilated in the high-latitude oceans, where they average the highly variable surface conditions, thereby providing an integrated measure of long-term trends. Here, we place the recent observations of OHC in the framework of long-term changes during the Holocene and the Common era.

We use a suite of sediment cores along bathymetric transects in the Makassar Strait and Flores Sea in Indonesia (figs. S1 and S2) to document changes in the temperature of western equatorial Pacific subsurface and intermediate water masses throughout the Holocene [0 to 10 thousand years before the present (ky B.P.)] (Table 1). This region is well suited to reconstruct Pacific OHC, as thermocline and intermediate water masses found here form in the mid- and high-latitudes of both the northern and southern Pacific Ocean and can be traced by their distinctive salinity and density as they flow toward the equator (7) (fig. S3). The Makassar Strait between Borneo and Sulawesi, the Lifamatola Passage east of Sulawesi on the northern side of the Indonesian archipelago, and the Ombai and Timor Passages to the south serve as major conduits for exchange of water between the Pacific and Indian Oceans; water flow through

[1]Institute for Marine and Coastal Sciences and Department of Earth and Planetary Sciences, Rutgers University, 71 Dudley Road, New Brunswick, NJ 08901, USA. [2]Lamont-Doherty Earth Observatory of Columbia University, Palisades, NY 10964, USA. [3]Department of Geology and Geophysics, Woods Hole Oceanographic Institution, Woods Hole, MA 02543, USA.

*Corresponding author. E-mail: rosentha@imcs.rutgers.edu

these passages is collectively referred to as the Indonesian Throughflow (ITF) (8). The upper thermocline component of the ITF (~0 to 200 m) is dominated by contributions from North Pacific and, to a lesser extent, South Pacific subtropical waters, marked by a subsurface salinity maximum (figs. S3 and S4). Within the lower thermocline (~200 to 500 m) the inflow of low-salinity North Pacific Intermediate Water (NPIW) dominates the ITF flow (fig. S4). The higher- and relatively uniform–salinity water below the main thermocline (~450 to 1000 m) is referred to as Indonesian Intermediate Water, which is formed in the Banda Sea by strong vertical mixing between shallow, warm, relatively fresh waters and deep, cold, relatively salty waters (8, 9). At intermediate depths, the Banda Sea gets contributions from the South Pacific through the northwestward-flowing New Guinea Coastal Undercurrent (NGCUC). Studies suggest that the NGCUC carries a substantial contribution from the Antarctic Intermediate Water, spreading into the Banda Sea through the Lifamatola and Makassar passages (10). The main subthermocline outflows through the Timor and Ombai passages reverse intermittently, thereby allowing inflow of Indian Ocean water into the Indonesian seas (8, 11, 12). Thus, the hydrography of intermediate water in this region is linked to and influenced by surface conditions in the high latitudes of the Pacific Ocean, as is also suggested from the distribution of anthropogenically produced chlorofluorocarbon along these isopycnal layers (7).

We studied well-dated sediment cores (table S1) in the Makassar Strait. Shallow cores (450 to 600 m) are used to reconstruct the hydrographic history of the lower thermocline, which currently is strongly influenced by NPIW. Deeper cores (650 to 900 m) from the Bali Basin on the western edge of the Flores Sea are arguably under greater influence of Southern Hemisphere (SH) water masses.

We use Mg/Ca measurements in the benthic foraminifer *Hyalinea balthica* for reconstructing intermediate water temperatures (IWTs). This species is ideally suited to track small temperature changes due to its high Mg/Ca-temperature sensitivity [Mg/Ca = (0.488 ± 0.03)·IWT] (13, 14). The error on IWT estimates is ±0.7°C for raw

data and ±0.35°C [one standard error of the estimate (SEE)] for composite records. The oxygen isotopic composition of seawater ($\delta^{18}O_{sw}$), used here as an analog for salinity, is estimated from the paired benthic foraminiferal oxygen isotopic composition ($\delta^{18}O_c$) and Mg/Ca data (15). Our reconstructions show that IWTs at all depths were substantially warmer in the early and middle Holocene than during the late Holocene (Fig. 1). Specifically, IWT at 500 m was ~10°C between 10.5 and 9 thousand years ago (ka), increased to a maximum of ~10.7°C between 8 to 6 ka, and began decreasing after 6 ka, reaching ~7.8°C at the core top (~100 years B.P.). In the 600-, 650-, and 900-m cores, a maximum IWT of ~8.2°C occurred between 10.5 and 9 ka and started decreasing after 9 ka, earlier than at the shallower site, reaching ~5.8°C at the core top (~100 to 300 years B.P.) (Table 1). The deepest site at 900 m shows an identical temperature trend with the 600- and 650-m sites. After correcting for sea-level rise from the early to mid-Holocene (15), we calculate Holocene cooling trends of ~2.2 ± 0.4°C and ~1.5 ± 0.3°C at 500 m and 600 to 900 m, respectively. Benthic foraminiferal $\delta^{18}O_c$ records at 600 and 650 m show a ~0.15 per mil increase from the middle to late Holocene and no major change at 500 m (fig. S5). These small changes cannot fully account for the cooling, thereby suggesting concomitant changes in salinity.

In contrast with the substantial IWT cooling, reconstructions of sea surface temperature (SST), based on Mg/Ca ratios in the mixed-layer foraminifer *Globigerinoides ruber* from multiple sites in the Indo-Pacific Warm Pool (IPWP), show only ~0.5°C cooling from ~9 ka to the 20th century (16) (Fig. 1). Mg/Ca records of the subsurface planktonic foraminifer *Pulleniatina obliquiloculata* that calcify at about 75- to 100-m depth (17, 18) suggest ~1.0°C cooling of the upper IPWP thermocline from the middle to the late Holocene (18–20). Thus, it seems that the Holocene subsurface cooling affected the water column below the mixed-layer and down to 900 m.

The early Holocene warmth and subsequent IWT cooling in Indonesia is likely related to temperature variability in the higher-latitude source waters. To assess the mechanisms that caused these hydrographic variations, we estimate down-core

Table 1. Core location and bottom water temperature and salinity at each site. Also given are the interval covered by each of the records, the average sedimentation rate, and the estimated core top ages. The "Period" column indicates maximum length. HL, Holocene length. psu, practical salinity units.

Site	Lat.	Long.	Depth (m)	Temp. (°C)	Salinity (psu)	Period	Avg. sed. rate (cm/ky)	Estimated core top age (year CE)
				Makassar Strait				
31MC/32GGC	3° 53.00'S	119° 27.24'E	455	8.1	34.481	CE	180	1990/1950
70GGC	3° 24.40'S	119° 23.41'E	482	7.8	34.500	HL	40	1900
34GGC	3° 53.16'S	119° 26.47'E	503	7.5	34.512	CE	180	1930/1600
47MC/48GGC	3° 53.30'S	119° 25.66''E	605	6.7	34.539	CE	150	1940/1640
				Flores Sea				
13GGC	7° 22.04'S	115° 12.72'E	594	6.5	34.547	HL	60	1830
10GGC	3° 24.54'S	115° 15.56'E	649	6.1	34.553	HL	50	1650
6MC/7GGC	7° 28.24'S	115° 21.53'E	920	5.2	34.583	HL/CE	75	1980/1600

salinities and densities for the 500- and 600- to 650-m depths. A temperature-salinity-density plot suggests that although the water masses were significantly warmer during the early middle Holocene than the late Holocene, their densities remained relatively constant throughout the Holocene (fig. S6). Thus, Holocene IWT cooling must have been largely compensated by freshening at the high-latitude source regions.

Intermediate water temperature records exhibit a Holocene thermal maximum (HTM) and Neoglacial cooling known from various terrestrial and marine records of the Northern Hemisphere (NH) and the SH [e.g., (1, 21–23)]. We compare our IWT anomalies with a recently published compilation of surface temperature records (23, 24). The anomalies are calculated relative to the reference period of 1850 to 1880 CE, as determined from the companion multicore records at each site (Fig. 2). Between 9 and 6 ka, the 500-m IWT trends resemble the NH surface high-latitude reconstruction (24), suggesting that the

HTM was 2.5 ± 0.4°C warmer than in the late 20th century. This is consistent with the surface estimate of 2.1 ± 0.2°C for the 30°N to 90°N latitudinal belt and is more than double the global ~0.7°C trend (24). The records from the deeper (600- to 900-m) sites, which arguably receive greater contributions from the SH, indicate that the IWT was 1.5 ± 0.4°C warmer during the HTM than the late 20th century. In contrast, the recent surface temperature reconstruction for the 30°S to 90°S band does not show a discernible trend throughout the Holocene (24). The discrepancy between our deep IWT record and the SH reconstruction might be due to the limited number of records used in the SH reconstruction and the uncertainty associated with estimating temperatures from ice-core records (24). Due to the strong vertical mixing in the Banda Sea, we cannot rule out the possibility that our 600- to 900-m IWT records were also primarily affected by North Pacific waters; however, we note the consistency with records showing Holocene cooling of ~1°C

to 2°C of SST north and south of the South Pacific Subtropical Convergence (23). The similarity between these SSTs and our IWT trends supports the proposed link to SH climate. The similar IWT trends observed between 480 and 900 m suggest that on orbital time scales, changes in Pacific OHC are largely determined by climate changes in the high latitudes that possibly respond to changes in the tilt of Earth's axis since the early Holocene (24). Changes in the seasonal cycle of the high latitudes, driven by Earth's precession, might be expected to affect the formation and heat-exchange rate of intermediate water masses. However, the similar cooling at intermediate depths influenced by both northern- and southern-sourced water masses, despite the antisymmetry in the precessional forcing, suggests that on these time scales, Earth's obliquity exerts the dominant influence on high-latitude temperatures and that OHC is highly sensitive to the changes at these latitudes. Although the exact mechanism is still unresolved, based on our density reconstructions we suggest that small perturbations in high-latitude climate are efficiently transferred to the ocean's interior along isopycnal surfaces, largely by density-compensated temperature changes, a mechanism proposed to explain modern observations (25). Over a long time, the ocean's interior acts like a capacitor and builds up large (positive and negative) heat anomalies that reflect and, more importantly, affect the global climate. We posit that the cooling of the thermocline and, to a lesser extent, the surface water in the IPWP (16), which is apparently at odds with model simulations forced by changes in insolation and atmospheric CO_2 throughout the Holocene, might have been caused by upward mixing of intermediate water in the Indonesian seas.

Multi- and gravity cores provide a record of IWT variability during the past two millennia. Because there is no major difference between the records at ~500, 600, and 900 m (fig. S7), we averaged these three records (Fig. 3). During the Common era, centennial IWT variability (500 to 900 m) is coherent with and closely follows changes in the overlying SST (26) and the NH (27, 28). IPWP SSTs are within error of modern (~1950 CE) values between 900 and 1200 CE during the Medieval Warm Period (MWP) and are colder by 0.75 ± 0.35°C between 1550 and 1850 CE during the Little Ice Age (LIA), followed by nonmonotonic warming in the past 150 years (26). Concomitantly, Pacific IWT was 0.9 ± 0.35°C (1 SEE) warmer during the MWP than during the LIA. Within age-model errors, the cooling trend from the MWP to LIA is of the same magnitude as, but possibly lags, the cooling of the overlying surface water and the NH. However, whereas the NH reconstructions (27, 28) show general nonmonotonic warming of ~0.5 ± 0.15°C for the period of 1850 to 1950 CE, which is consistent with the instrumental record for the NH (24°N to 90°N) during the same period (29), we see no significant change in IWT (ΔIWT = 0.15 ± 0.35°C) between 1850 and 1950 CE (Fig. 3).

Fig. 1. Down-core records from sites in the IPWP. (A) Mg/Ca-derived SST from the Makassar Strait (70GGC, red), Flores Sea (13GGC, gray), and Timor Sea (MD78, magenta) (16, 18). **(B)** Mg/Ca-derived thermocline water temperature (TWT) from sites in the Timor Sea (18), Philippines Sea (20), and northern South China Sea (19) (see fig. S2 for map of sites). **(C)** Intermediate water temperatures from the Indonesian bathymetric transect. **(D)** Bottom water $\delta^{18}O_{sw-iv}$ corrected for ice volume (iv) effect. Age models for the records are based on accelerator mass spectrometry ^{14}C dating (table S1) and marked with triangles at the bottom. ^{14}C date color coding is as shown in the bottom key. S.L., sea level; SMOW, standard mean ocean water; ‰, per mil.
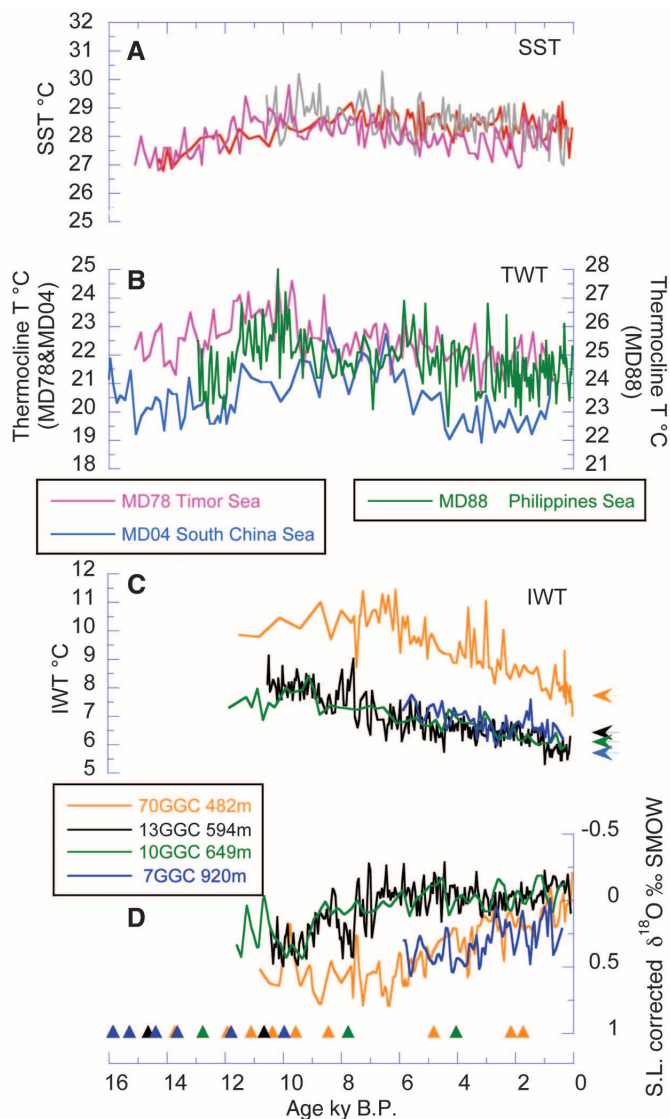
The difference between the IWT and SST estimates in the same core and elsewhere likely reflects the fact that it takes several decades for the intermediate water masses to reach the western equatorial Pacific from their high-latitude origins (7). To the extent that our reconstruction reflects high-latitude climate conditions in both hemispheres, it differs considerably from the recent

surface compilations, which suggest ~2°C MWP-to-LIA cooling in the 30°N to 90°N zone, whereas the 30°S to 90°S zone warmed by ~0.6°C during the same interval (24). In contrast, our composite IWT records of water masses linked to NH and SH water masses imply similar patterns of MWP-to-LIA cooling at the source regions The inferred similarity in temperature anomalies at both hemi-

spheres is consistent with recent evidence from Antarctica (30), thereby supporting the idea that the HTM, MWP, and LIA were global events. Furthermore, the similar expressions in both hemispheres indicate a strong link to global radiative perturbations rather than a regional response to changes in ocean circulation.

With no additional IWT records, it is difficult to assess the global extent of the trends we have reconstructed. Instead, we evaluate the possible implications for Pacific OHC at four discrete periods during the Holocene. We consider three sensitivity cases, whereby the observed IWT trends in Indonesia are applied to 25, 50, and 75% of the Pacific volume between 0 and 700 m (15) (Fig. 4). The reconstructed OHC is compared with modern observations for the whole Pacific at the same depth range (5). The comparison suggests that Pacific OHC was substantially higher during most of the Holocene than in the past decade (2000 to 2010), with the exception of the LIA. The difference is statistically significant, even if the OHC changes apply only to
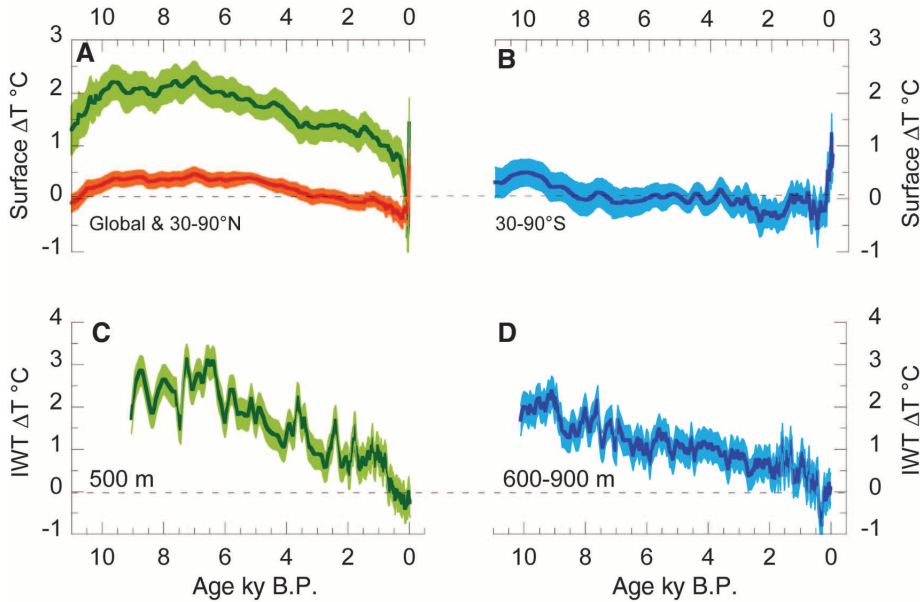

Fig. 2. Comparison between Holocene reconstructions of surface and intermediate-water temperatures. (**A**) Global (red) and 30°N to 90°N (green) surface temperatures anomalies, (**B**) 30°S to 90°S surface temperature anomalies (24), (**C**) changes in IWT at 500 m, and (**D**) changes in IWT at 600 to 900 m. All anomalies are calculated relative to the temperature at 1850 to 1880 CE. Shaded bands represent ±1 SD. Note the different temperature scales.

Fig. 3. Temperature anomaly reconstructions for the Common era relative to the modern data (note that the age scale is in Common era years with the present on the right). (**A**) Change in SST from the Makassar Straits [orange, based on (26) compared with NH temperature anomalies (27, 28)]. (**B**) Compiled IWT anomalies based on Indonesian records spanning the ~500- to 900-m water depth (for individual records, see fig. S7). The shaded band represents ±1 SD.

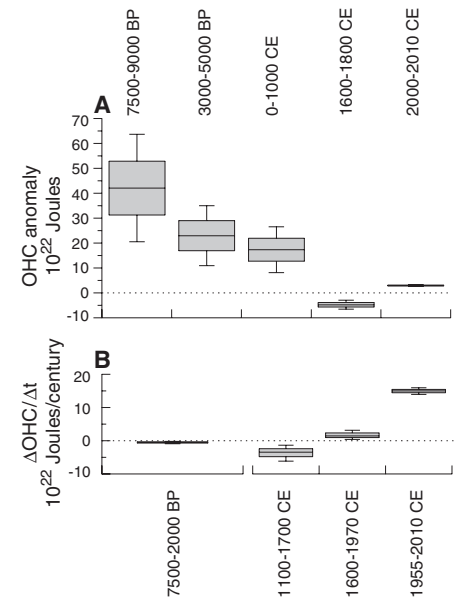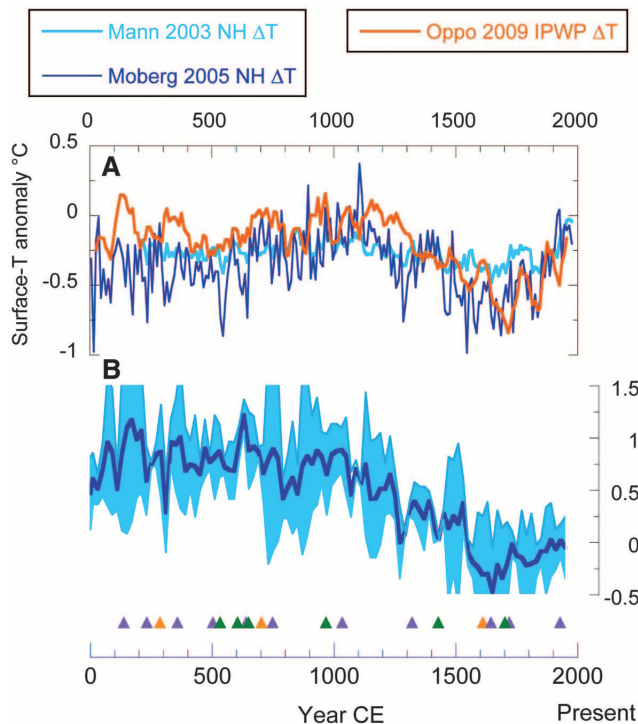**Fig. 4. Holocene changes in Pacific Ocean heat content.** (**A**) Reconstructed anomalies in Pacific OHC in the 0- to 700-m depth interval for the early Holocene, mid-Holocene, MWP, and LIA periods. Reconstructed anomalies are calculated relative to the reference period of 1965 to 1970 CE (15). (**B**) Reconstructed rates of OHC change during the main transition periods. Reconstructed anomalies and rates are compared with modern observations for the 2000 to 2010 and 1955 to 2010 CE periods, respectively (5). The middle line at each box represents an average estimate for 50% of the Pacific volume between 0 and 700 m, whereas the top and bottom quartiles of the box represent 62.5 and 37.5% of the total volume in this depth interval, respectively. The bottom whiskers represent 25% of the volume; the top whisker denotes 75%. The modern value is based on the entire Pacific volume for 0 to 700 m.

the western Pacific (~25% Pacific volume), although there are indications that similar trends extended farther east ([15]). The modern rate of Pacific OHC change is, however, the highest in the past 10,000 years (Fig. 4 and table S3).

The current response of surface temperatures to the ongoing radiative perturbation is substantially higher than the response of the ocean's interior, due to the long whole-ocean equilibration time. However, on longer time scales the oceanic response is likely different, as seen in our records where past changes in IWT were much larger than variations in global surface temperatures. The large variations in IWT and inferred OHC during the Holocene and Common era, when global temperature anomalies were relatively small, imply elevated sensitivity to climate conditions in the high latitudes, which, on a multidecadal scale, likely enables the ocean to mediate perturbations in Earth's energy budget.

References and Notes

1. H. Wanner et al., Quat. Sci. Rev. 27, 1791–1828 (2008).
2. L. Leduc, R. Schneider, J.-H. Kim, G. Lohmann, Quat. Sci. Rev. 29, 989–1004 (2010).
3. D. R. Easterling, M. F. Wehner, Geophys. Res. Lett. 36, L08706 (2009).
4. S. Levitus, J. Antonov, T. P. Boyer, C. Stephens, Science 287, 2225–2229 (2000).
5. S. Levitus et al., Geophys. Res. Lett. 39, L10603 (2012).
6. J. Hansen et al., Science 308, 1431–1435 (2005).
7. R. A. Fine, R. Lukas, F. M. Bingham, M. J. Warner, R. H. Gammon, J. Geophys. Res. 99, 25063–25080 (1994).
8. A. Gordon, Oceanography 18, 14–27 (2005).
9. L. D. Talley, J. Sprintall, J. Geophys. Res. 110, C10009 (2005).
10. W. Zenk et al., Prog. Oceanogr. 67, 245–281 (2005).
11. S. Wijffels, J. Sprintall, M. Fieux, N. Bray, Deep Sea Res. Part II Top. Stud. Oceanogr. 49, 1341–1362 (2002).
12. J. Sprintall, S. E. Wijffels, R. Molcard, I. Jaya, J. Geophys. Res. 114, C07001 (2009).
13. Y. Rosenthal et al., Geophys. Geochem. Geosys. 12, 1–17 (2011).
14. A. Morley et al., Earth Planet. Sci. Lett. 308, 161–171 (2011).
15. Supplementary materials are available on Science Online.
16. B. K. Linsley, Y. Rosenthal, D. W. Oppo, Nat. Geosci. 3, 578–583 (2010).
17. M. Mohtadi et al., Paleoceanography 26, PA3219 (2011).
18. J. Xu, A. Holbourn, W. Kuhnt, Z. Jian, H. Kawamura, Earth Planet. Sci. Lett. 273, 152–162 (2008).
19. S. Steinke et al., Global Planet. Change 78, 170–177 (2011).
20. H. Dang, Z. Jian, F. Bassinot, P. Qiao, X. Cheng, Geophys. Res. Lett. 39, 1–5 (2011).
21. V. Masson et al., Quat. Res. 54, 348–358 (2000).
22. P. A. Mayewski et al., Quat. Res. 62, 243–255 (2004).
23. H. C. Bostock et al., Quat. Sci. Rev. 74, 35–57 (2013).
24. S. A. Marcott, J. D. Shakun, P. U. Clark, A. C. Mix, Science 339, 1198–1201 (2013).
25. C. Mauritzen, A. Melsom, R. T. Sutton, Nat. Geosci. 5, 905–910 (2012).
26. D. W. Oppo, Y. Rosenthal, B. K. Linsley, Nature 460, 1113–1116 (2009).
27. M. E. Mann et al., Proc. Natl. Acad. Sci. U.S.A. 105, 13252–13257 (2008).
28. A. Moberg et al., Nature 433, 613–617 (2005).
29. T. M. Smith, R. W. Reynolds, T. C. Peterson, J. Lawrimore, J. Clim. 21, 2283–2296 (2008).
30. A. J. Orsi, B. D. Cornuelle, J. P. Severinghaus, Geophys. Res. Lett. 39, 1–7 (2012).

Reconstructing the Microbial Diversity and Function of Pre-Agricultural Tallgrass Prairie Soils in the United States

Noah Fierer,[1,2]* Joshua Ladau,[3] Jose C. Clemente,[4] Jonathan W. Leff,[1,2] Sarah M. Owens,[5,6] Katherine S. Pollard,[3,7] Rob Knight,[8,9] Jack A. Gilbert,[5,10] Rebecca L. McCulley[11]

Native tallgrass prairie once dominated much of the midwestern United States, but this biome and the soil microbial diversity that once sustained this highly productive system have been almost completely eradicated by decades of agricultural practices. We reconstructed the soil microbial diversity that once existed in this biome by analyzing relict prairie soils and found that the biogeographical patterns were largely driven by changes in the relative abundance of Verrucomicrobia, a poorly studied bacterial phylum that appears to dominate many prairie soils. Shotgun metagenomic data suggested that these spatial patterns were associated with strong shifts in carbon dynamics. We show that metagenomic approaches can be used to reconstruct below-ground biogeochemical and diversity gradients in endangered ecosystems; such information could be used to improve restoration efforts, given that even small changes in below-ground microbial diversity can have important impacts on ecosystem processes.

After the European settlement of the midwestern United States in the mid-19th century, the tallgrass prairie ecosystem was profoundly altered by the removal of key animal taxa (including bison), fire suppression, and the plowing under of native grasses. Together these land-use changes contributed to the most substantial decline of any major ecosystem in North America ([1, 2]). This ecosystem, which once covered nearly 10% of the contiguous United States (>65 million ha), has been reduced to a small fraction of its historical extent ([3]). Cultivation and row crop agriculture, now practiced across most of the tallgrass prairie biome, not only replaced species-rich plant communities with monoculture croplands, but also drastically altered the physicochemical and biological characteristics of prairie soils. Except for a few prairie relicts that have never been tilled, the soils currently found throughout the region bear little resemblance to their pre-agricultural state ([4–7]). We confirmed the effect of cultivation on soil microbial communities by directly comparing bacterial communities in cultivated soils with paired uncultivated soils collected from throughout the native tallgrass prairie range (table S1), and found that the cultivated soils harbored bacterial communities that were significantly distinct in composition from those found in the corresponding native prairie soils (fig. S1).

Owing to the historical and biological importance of the native tallgrass prairie, there have been various attempts to predict the historical distributions of plants and animals across this ecosystem [e.g., ([8])]. However, comparable reconstructions of below-ground microbial diversity have, to our knowledge, never been attempted, hindering our understanding of how soil microbes may have once influenced plant production, nutrient retention, and soil carbon dynamics in this ecosystem. By coupling metagenomic sequence data, which capture the phylogenetic and functional diversity of existing soil microbial communities ([9, 10]) found in tallgrass prairie remnants, to spatially explicit models ([11]), which predict the structure

[1]Department of Ecology and Evolutionary Biology, University of Colorado, Boulder, CO 80309, USA. [2]Cooperative Institute for Research in Environmental Sciences, University of Colorado, Boulder, CO 80309, USA. [3]The Gladstone Institutes, University of California, San Francisco, CA 94158, USA. [4]Department of Genetics and Genomic Sciences and Department of Medicine, Mount Sinai School of Medicine, New York, NY 10029, USA. [5]Institute of Genomic and Systems Biology, Argonne National Laboratory, Argonne, IL 60439, USA. [6]Computation Institute, University of Chicago, Chicago, IL 60637, USA. [7]Institute for Human Genetics and Division of Biostatistics, University of California, San Francisco, CA 94143, USA. [8]Department of Chemistry and Biochemistry, University of Colorado, Boulder, CO 80309, USA. [9]Howard Hughes Medical Institute, Boulder, CO 80309, USA. [10]Department of Ecology and Evolution, University of Chicago, Chicago, IL 60637, USA. [11]Department of Plant and Soil Sciences, University of Kentucky, Lexington, KY 40546, USA.

*Corresponding author. E-mail: noah.fierer@colorado.edu